Author:

Mingteng Tian(12432250@mail.sustech.edu.cn),

Southern Univesity of Science and Technology, Shenzhen, China

Yingjie Yang(yangyj@sustech.edu.cn),

Southern Univesity of Science and Technology, Shenzhen, China

DispSAC: Surface-wave dispersion inversion using soft actor-critic reinforcement learning

Mingteng Tian[1], Yingjie Yang[1]

[1]Department of Earth and Space Sciences, Southern University of Science and Technology, Shenzhen, China

Abstract

Surface-wave inversion (SWI) is widely used to image shear-wave velocity structure in the crust and upper mantle. Locally linearized methods offer computational efficiency but can be sensitive to the initial model and regularization, whereas Bayesian sampling methods can characterize model uncertainty at substantial computational cost. Neural networks provide another route to efficient inversion, although deterministic predictions alone do not describe the range of models compatible with the data. We present DispSAC, an iterative SWI method based on the off-policy soft actor-critic reinforcement-learning algorithm. The agent is trained using synthetic Rayleigh-wave dispersion curves generated from isotropic shear-wave velocity models parameterized by B-splines. During inference, the trained policy repeatedly updates the model parameters using feedback from a physical forward solver. Multiple initializations produce an ensemble of recovered models whose spread describes variability among the solutions obtained. We evaluate DispSAC using synthetic test data drawn from the training distribution, synthetic data derived from a western United States reference model, and observed dispersion data from Yunnan, China. The results demonstrate that the learned policy can reduce dispersion misfit across these datasets and recover regional velocity structure. Comparisons with the implemented Markov chain Monte Carlo baseline suggest potential computational benefits under the tested conditions. DispSAC offers a sufficiently generalized framework for reusing inversion experience across locations and for future integration with additional geophysical observations.

Keywords: surface-wave inversion; shear-wave velocity; reinforcement learning; soft actor-critic; inverse problems; seismological imaging

Code availability: https://github.com/MingtengTian/DispSAC.git

Introduction

Surface waves are widely used to image subsurface shear-wave velocity structure across a broad range of spatial scales, from the near surface to the crust and upper mantle. Surface-wave dispersion measurements can be obtained from both earthquake records and ambient seismic noise. A central step in surface-wave imaging is the inversion of these measurements for shear-wave velocity, V_s, as a function of depth.

Methods for inverting surface-wave dispersion curves include locally linearized approaches, Bayesian sampling, and global optimization [4]. Locally linearized approaches use an objective function and its derivatives to update the velocity model. These methods can be efficient, but their results may depend on the initial model and the choice of regularization [5]. Bayesian approaches, commonly implemented using Markov chain Monte Carlo (MCMC), explore models according to a specified posterior distribution [31, 32, 35, 37, 39]. Global optimization methods, such as particle swarm optimization (PSO), instead search for models that minimize an objective function [34]. Both sampling and global optimization can explore a broader region of parameter space than a local update scheme, although their performance remains dependent on the parameterization and search configuration. When inversions are performed independently at many locations, the repeated forward calculations can require substantial computational effort.

Deep-learning methods have been investigated as alternatives to repeated optimization, with the aim of improving the efficiency of geophysical inversion [6]. Approaches include feedforward neural networks [7, 8], long short-term memory networks [4], convolutional neural networks [33], transformers [6], physics-informed neural networks [1], generative adversarial networks [19] and deep learning-based surrogate model [30]. Their objectives and outputs differ, and some address surface-wave tomography rather than local dispersion inversion. A deterministic network that returns a single velocity model for each dispersion curve provides a point estimate; that estimate alone does not characterize the non-uniqueness of the inverse problem. Its performance can also depend on how well the training data represent the observations encountered during application. Larger and more diverse synthetic datasets, such as OpenSWI [16], can support broader training coverage, but inferring performance on data outside the training distribution must still be assessed when discarding fintune process. These considerations motivate approaches that combine learned information with iterative evaluation of the physical data fit.

Reinforcement learning (RL) provides a framework for learning sequential decisions through interaction with an environment. An agent selects actions according to a policy and receives rewards that guide it toward a specified objective [20]. An inversion problem can be formulated as a Markov decision process (MDP) by defining a state, an action space, a transition mechanism, and a reward function [27, 41]. In this formulation, the state must contain the information needed to determine the consequences of the next action. RL-based approaches have been explored in full-waveform inversion [11], magnetotelluric inversion [14], and other geophysical applications [13, 38]. These studies motivate investigating whether a learned policy can guide successive model updates in SWI.

Our objective is to learn a model-update policy that can reuse information gained from previous inversions. Experience replay supports this objective by storing transitions and making them available for subsequent learning updates [28, 29]. Off-policy algorithms can learn from data collected under earlier policies, separating data collection from policy optimization. This reuse can improve sample efficiency relative to approaches that rely primarily on recent on-policy trajectories [24]. We therefore investigate soft actor-critic (SAC), an off-policy algorithm developed for continuous-control problems [22, 23]. Its stochastic policy and entropy-regularized objective provide a means of balancing exploration with reward maximization. These properties make SAC a suitable candidate for updating the continuous parameters of a surface-wave velocity model.

This study introduces DispSAC, which uses a trained SAC policy to guide iterative inversion of surface-wave dispersion data. The method combines a compact B-spline parameterization with a physical forward solver and applies the learned policy to previously unseen dispersion curves. We investigate its sensitivity to different initial models through repeated inversions and evaluate its performance on synthetic and observed datasets. Comparisons with an MCMC implementation examine model recovery, data fit, and computational cost under the selected experimental settings. The resulting framework may also support future joint inversion with receiver functions or other complementary observations.

Method

1. Synthetic data construction

We construct synthetic training data by calculating Rayleigh-wave dispersion curves from prescribed shear-wave velocity models. The crustal and upper-mantle velocity structure is represented using B-spline basis functions. This parameterization provides a compact description of smoothly varying structure within each modeled region and reduces the number of free parameters relative to a finely layered model. It is consistent with the broad depth sensitivity of surface-wave dispersion, while imposing assumptions about the range of structures that can be recovered.

We use four B-spline coefficients for the crust and five for the mantle to balance model flexibility and computational cost. A small number of coefficients reduces the dimension of the action and model spaces, but it can also limit the representation of sharp gradients or complex structures. The velocity profile is obtained by combining the coefficients with the corresponding B-spline basis functions, as expressed in Equation (1).

$$V_i = \sum_{j=1}^{m} c_j \, B_{ij}, \qquad i = 1, \ldots, n. \tag{1}$$

Here, c_j is the jth B-spline coefficient, B_ij is the jth basis function evaluated at the depth of layer i, m is the number of coefficients in the expansion, and n is the number of layers. V_i denotes the shear-wave velocity assigned to layer i.

To sample a range of velocity structures, we randomly generate B-spline coefficients within the bounds listed in Table 1. The resulting models define the synthetic training distribution. These bounds can be widened or narrowed to represent different structural ranges, although the chosen parameterization and sampling strategy continue to constrain the models encountered during training.

We generate 50,000 isotropic velocity models using randomly sampled B-spline coefficients and calculate their Rayleigh-wave dispersion curves with Computer Programs in Seismology (CPS) [21]. Forward calculations require layer thickness, shear-wave velocity, compressional-wave velocity, density, and attenuation parameters. Empirical relations between elastic-wave velocities and density are used following Brocher [40] in equation (2) and (3). Dispersion is calculated at 36 periods between 1 and 100 s, with the full period grid listed in Table 1. The resulting synthetic curves provide the target dispersion data used during training.

$$V_p = 0.941 + 2.095V_s - 0.821V_s^2 + 0.268V_s^3 - 0.0251V_s^4 \tag{2}$$

$$\rho = 1.227 + 1.53V_s - 0.837V_s^2 + 0.207V_s^3 - 0.0166V_s^4 \tag{3}$$

The synthetic dataset is divided into training (95%), validation (4.5%), and test subsets (0.5%). The training subset is used to optimize the agent, and the validation subset is used to monitor performance during training. The test subset is held out for evaluation after training. Training and validation misfit histories are compared to assess optimization progress and identify possible deterioration in generalization.

Table 1 Model-parameter bounds and periods used to generate the synthetic dispersion dataset.

Parameter	Range
Moho Depth	7–70 km
1st Crust Bspline Coefficient	2.2–4.0 km/s
2nd Crust Bspline Coefficient	3.0–4.2 km/s
3rd Crust Bspline Coefficient	3.5–4.2 km/s
4th Crust Bspline Coefficient	3.8–4.4 km/s
1st~5th Mantle Bspline Coefficient	4.0–5.0 km/s
Rayleigh-wave periods	1, 2, 3, 4, 5, 6, 7, 8, 9, 11, 13, 15, 17, 19, 22, 25, 28, 31, 32, 34, 37, 40, 43, 46, 49, 52, 55, 60, 65, 70, 75, 80, 85, 90, 95, 100 s

2. Training framework

In the RL formulation, the agent observes a state s_t at step t and selects an action a_t according to a policy $\pi(a_t \mid s_t)$. The environment then returns a scalar reward r_t and a new state s_{t+1} according to its transition dynamics. The discount factor γ, with $0 \leq \gamma < 1$, controls the relative contribution of future rewards to the expected return. SAC augments reward maximization with an entropy term that encourages policy exploration [22, 23].

For SWI, the agent learns a sequence of parameter updates that improves the fit between predicted and target dispersion. The state includes the current model parameters, information about the dispersion mismatch, and the progress of the inversion. An action modifies the parameter vector, from which a new velocity profile is constructed. The forward solver then calculates the corresponding dispersion, allowing the environment to update the state and reward. Through repeated interaction, the policy learns to select model updates that improve the cumulative inversion objective.

The training framework comprises an environment, an actor, two critics, an entropy-temperature parameter, and a replay buffer.

The environment applies the proposed parameter update, constructs the velocity model, and evaluates its predicted dispersion using CPS. It then calculates the dispersion misfit and returns the updated state and reward. To reduce file input/output overhead during repeated forward evaluations, the Fortran forward routines are compiled and integrated into the inversion environment. The same forward-calculation implementation is used for the DispSAC and MCMC comparisons.

The actor represents the policy that maps the current state to an action. Its input includes dispersion information, the current model parameters, the dispersion mismatch, and the inversion step. The action specifies an increment to the model-parameter vector. Applying this increment produces the next candidate model, whose dispersion is evaluated by the environment.

The critics estimate the soft action value associated with a state-action pair, accounting for the expected future rewards and the entropy contribution under the policy. SAC uses two critic networks and their lower value estimate in the relevant learning targets to reduce overestimation bias. The actor is updated using these value estimates, whereas the environment supplies the reward associated with each model update [22, 23].

The entropy temperature determines the weight of the entropy term in the SAC objective. A larger weight favors a more exploratory policy, whereas a smaller weight places greater emphasis on maximizing the expected reward. This balance influences how broadly the agent explores possible model updates during training. It does not, by itself, guarantee convergence to a global optimum.

The replay buffer stores transitions collected during interaction with the environment. Batches of these transitions are sampled to update the actor and critic networks and, when temperature optimization is enabled, the entropy-temperature parameter. In the replay scheme described here, lower dispersion misfit is assigned higher sampling priority, increasing the frequency with which well-fitting transitions are revisited during training.

Training uses an NVIDIA A100 GPU for neural-network optimization and CPU resources for the repeated forward calculations. This division assigns the matrix operations involved in backpropagation to the GPU while allowing the forward-modeling workload to be distributed across CPU workers.

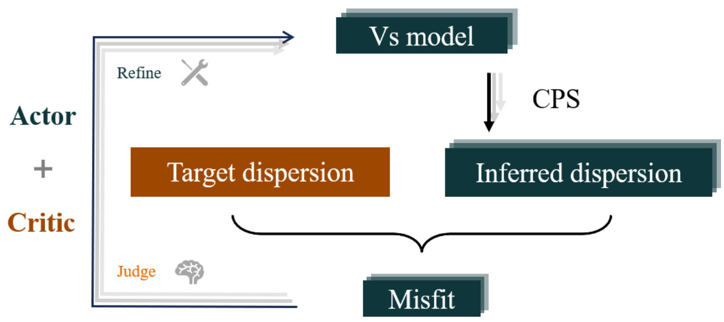

Figure 1 DispSAC inference workflow. Critic and actor can be considered as the 'brain' and 'hand' of the agent respectively. Critic is responsible for juduging if the path is promising from misfit and actor is responsible for refining vs model.

3. Inference procedure

After training, the learned policy is applied to previously unseen dispersion curves to iteratively estimate the corresponding shear-wave velocity models. During inference, the neural-network parameters remain fixed. Only the geophysical model parameters are updated according to the actions generated by the trained policy.

We evaluate inference in three settings. First, synthetic test curves drawn from the same generation procedure as the training data assess performance within the training distribution. Second, synthetic curves derived from a western United States reference model assess transfer to a separately constructed regional dataset. Third, observed dispersion curves from ambient-noise measurements in Yunnan, China, assess application to field data with more variable coverage and measurement quality.

Result

1. Training performance

The agent is trained on the synthetic dispersion dataset described above. Each rollout contains 20 environment steps, with one forward evaluation per step. Each target dispersion curve is retained for three successive rollouts, giving 60 environment steps per target, as specified by Equation (4). After the initial warm-up stage, the reported configuration performs 16 learning updates per environment step. Increasing this replay ratio allows greater reuse of collected transitions [24], although it also increases optimization work and may affect learning stability.

$$S_{\text{total}} = PS_r \tag{4}$$

Here, S_{total} is the number of environment steps allocated to each target dispersion curve, P is the number of consecutive rollouts using that target, and S_r is the number of steps in each rollout. In the reported configuration, $P = 3$ and $S_r = 20$, giving $S_{total} = 60$.

Observed dispersion measurements can contain errors arising from data acquisition, signal processing, and curve picking. We adopt a nominal relative noise level of approximately 1% as an experimental assumption. Figure 2 shows that the training and validation misfits decrease during training and become more stable at later updates. The final values annotated in the figure are 0.0099 and 0.0131 km/s, respectively. The misfit measure and its phase- and group-velocity contributions are defined in Equations (5) and (6).

$$M = \sqrt{\frac{1}{N}\sum_{k=1}^{N}\left(v_k^{\text{pred}} - v_k^{\text{obs}}\right)^2}. \tag{5}$$

$$M_{\text{total}} = w_c M_{\text{phase}} + w_U M_{\text{group}}. \tag{6}$$

Here, v_k^{obs} and v_k^{pred} are the target and predicted velocities at the kth period, respectively, and N is the number of valid period samples. Equation (6) is evaluated separately for phase velocity and group velocity. The nonnegative weights w_c and w_U control their contributions to the total misfit. The misfit has units of km/s when the velocity measurements are expressed in km/s and the weights are dimensionless. Morevoer, N is given as 36 and w_U is zero because we ignore group velocity in this study.

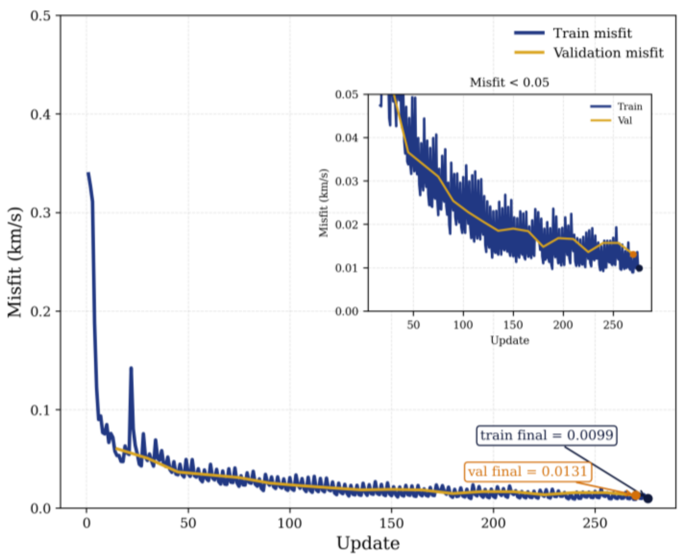

Figure 2 Training Curve of DispSAC. The spikes in the training diagram mean the transition of datasets between old batches and new batches. Every batch handles 96 diseprsion datasets that are distributed to 96 CPUs for forward simulations.

2. Evaluation on synthetic test data

We first apply the trained DispSAC agent to the held-out synthetic test curves. These curves are generated using the same procedure as the training data and therefore provide an evaluation within the specified training distribution.

For each target curve, the learnt policy starts from a randomly initialized parameter vector and updates it over a 20-step rollout. At each step, the revised parameters define a velocity model whose predicted dispersion is compared with the target. Repeating the procedure from multiple initializations produces an ensemble of recovered velocity profiles and their corresponding dispersion curves. We summarize these results using ensemble means and the spread among the recovered models. A close dispersion fit indicates consistency with the target data, but the non-uniqueness of SWI means that it does not necessarily imply perfect recovery of the exact target velocity profile for every single inference.

Multiple initializations allow us to examine the variability of the solutions obtained by the learned policy. Each initialization defines an independent inversion trajectory containing 20 model-update steps. A prescribed dispersion-misfit threshold around 2%~3% dispersion velocity value can be used to identify acceptable solutions. The spread of the retained models describes variability within the resulting ensemble and may provide a useful measure of sensitivity to initialization.

Figure 3 illustrates one inversion trajectory, showing the evolution of the velocity profile and its predicted dispersion over 20 steps. Figure 4 summarizes 100 inversions of the same target curve from different initial models. Panels (a) and (b) show the recovered profiles and dispersion curves, panel (c) shows the depth-dependent standard deviation of the recovered velocities, and panel (d) shows the misfit histories. Decreasing misfit makes predicted dispersions approximate closer to the target dispersion followed by predicted velocity models approximate closer to target model. The misfit decreases overall in the big picture, although some trajectories exhibit temporary increases before the end of the rollout. The misfit decrease after temporary increase proofs that the trained policy might skip the local minimum. According to misfit histories, no matter how great the initial misfits are, the trained policy can decrease misfit to the accepted threshold.

These results support the applicability of DispSAC to held-out synthetic curves generated within the training distribution. Evaluation on independently constructed regional data is needed to assess how the learned policy transfers beyond this setting.

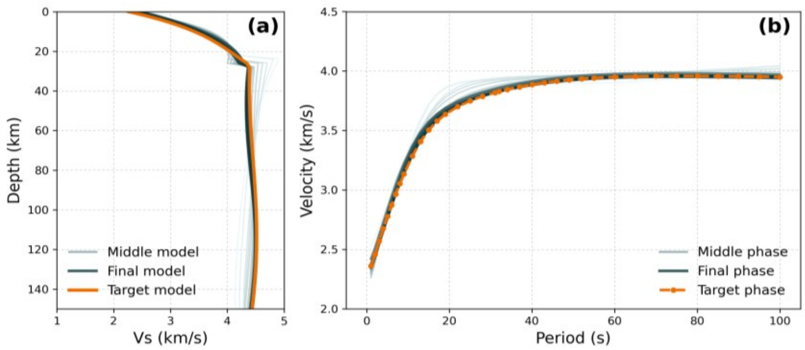

Figure 3 Inferring synthetic test dispersions. (a) v_s changes in one rollout (20 steps) when inferring dispersion, including target v_s model and middle step v_s models; (b) The corresponding dispersion of v_s models in (a), including target dispersion and middle step dispersions;

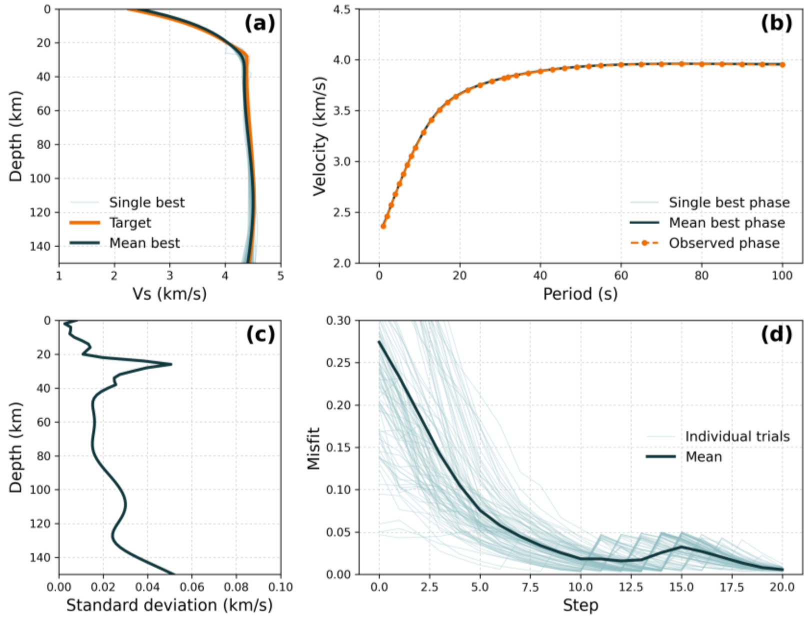

Figure 4 Inferring synthetic test dispersions. (a) All final v_s models of 100 different random initializations after their rollouts and the averaged predicted v_s model of all 100 final v_s models; (b) All final dispersions of 100 different random initializations after their rollouts and the averaged predicted dispersion of all 100 final dispersions; (c) The standard diviation of all 100 final best inversions; (d) Mean misfit changes of all 100 inferences.

3. Evaluation on western United States synthetic data

To evaluate transfer to a separately constructed regional dataset, we generate synthetic Rayleigh-wave dispersion curves from a western United States reference model ([12]). The region contains substantial lateral variations in crustal and upper-mantle velocity structure, providing a useful setting for examining the performance of the trained policy across different structural conditions.

For each regional target curve, we perform 100 inversions from randomly initialized parameter vectors. Each inversion contains a 20-step rollout. The recovered parameter vectors are converted into velocity profiles using the B-spline representation, and their ensemble mean is used to summarize the result at that location. Figures 5 and 6 illustrate an individual target, while Figure 7 compares regional velocity maps at selected depths.

Figure 6 shows the ensemble inversion results at 254.5°E, 30.75°N. Panel (a) compares the target velocity profile with the recovered profiles and their mean, and panel (b) compares the corresponding dispersion curves. Panel (c) shows the standard deviation of V_s at each depth across the recovered models. Panel (d) shows the individual and mean dispersion-misfit histories over the 20-step rollouts.

Figure 7 shows that DispSAC reproduces the main features of the reference model, with small velocity deviations that change sign with depth. Overestimation at some depths and underestimation at others may partly compensate in their effects on dispersion, allowing a close dispersion fit despite differences between the recovered and target velocity profiles. This behavior is consistent with depth-dependent parameter trade-offs and the non-uniqueness of surface-wave inversion.

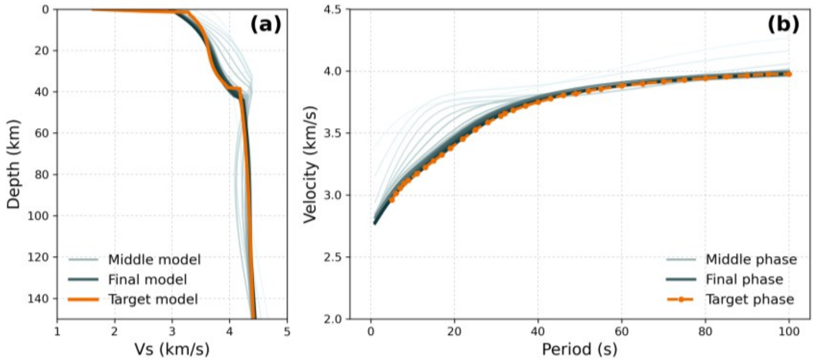

Figure 5 One inference of synthetic Rayleigh dispersion in Western US's grid 254.5E, 30.75N. (a) v_s changes in one rollout (20 steps) when inferring dispersion, including target v_s model and middle step v_s models; (b) The corresponding dispersion of v_s models in (a), including target dispersion and middle step dispersions;

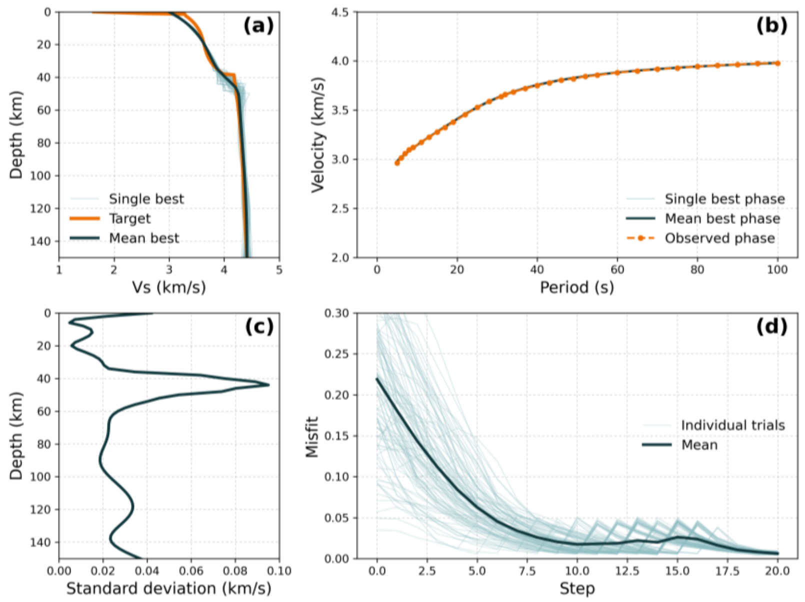

Figure 6 100 inferences of synthetic Rayleigh dispersion in Western US's grid 254.5E, 30.75N. (a) All final 100 possible v_s model predictions and the averaged v_s model prediciton;(b) All final 100 possible dispersion predictions and the averaged dispersion prediction; (c) The misfit standard diviation of all 100 final best inversions; (d) Mean misfit changes of all 100 inferences.

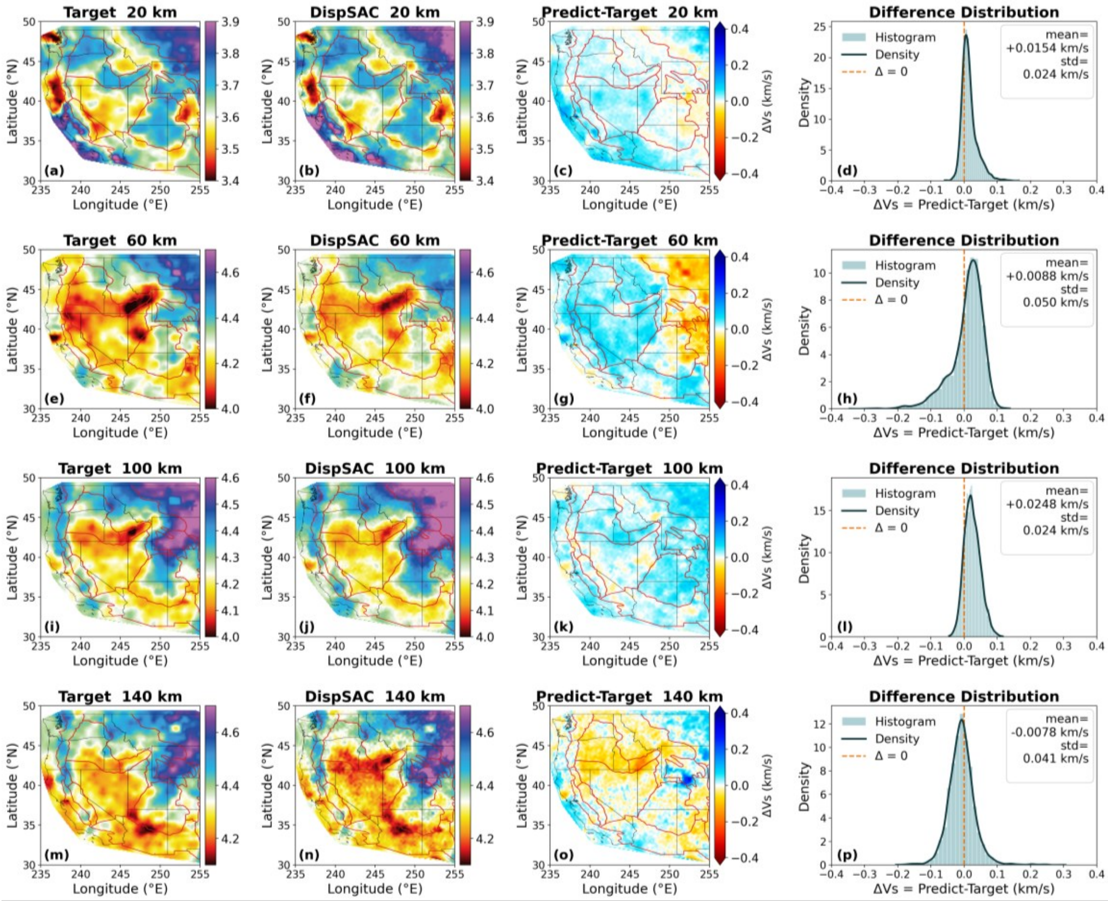

Figure 7 Comparison between target Western US v_s model and the DispSAC inferred v_s model in 20km, 60km, 100km and 140km. First column: (a), (e), (i) and (m) means the Target Western US v_s model; Second column: (b), (f), (j) and (n) means DispSAC prediction; Third column: (c), (g), (k) and (o) mean the difference between prediction and target; Fourth column: (d), (h), (l) and (p) is the difference distribution between DispSAC prediction and target.

4. Application to Yunnan observations

Observed dispersion curves differ from the synthetic training data in their period sampling, usable period range, and measurement errors. We interpolate measurements onto the training period grid within the observed coverage. To improve tolerance to incomplete curves, training augmentation randomly removes samples from the short-period end, the long-period end, or both ends of a curve. Gaussian noise is also added during training to expose the agent to perturbed observations. These procedures are intended to improve performance on variable data coverage and noise conditions, but their effectiveness depends on how well the augmentations represent the field data. Measurements outside the usable period range remain unconstrained by the observations.

For each Yunnan target curve, we initialize 2,500 parameter vectors and apply the trained policy to update the associated velocity models by setting the final phase misfit threshold as 0.1, which accepts final dispersion misfit within roughly 3%. The recovered parameters are converted into velocity profiles using the B-spline representation, and the profiles are averaged to summarize the result at each location. For comparison, the same dispersion data are inverted using an MCMC implementation, with 2,500 retained models used to summarize its results. Figure 8 compares the velocity fields recovered by the two methods at selected depths.

Figures 9 and 10 compare the phase-velocity residuals obtained with DispSAC and MCMC at periods of 10, 20, 30, 40, 60, and 80 s. The histograms show their distributions, and the maps show their spatial patterns. The distributions indicate differences in both residual spread and bias, with the degree of agreement varying across periods. These comparisons assess the fit to the observed dispersion data; they can not estimate which inferred velocity field is closer to the Earth structure because there are no ground truth of real data.

Figure 11 compares the recorded computational costs of the two methods for the Yunnan dataset. The displayed times are 37.1 min for DispSAC and 1.17 h for MCMC for the single-curve benchmark, and 2.53 and 4.79 h, respectively, for the full dataset. These results indicate shorter elapsed inference times for DispSAC in the reported runs. Their interpretation depends on the hardware, parallelization, initialization, and stopping criteria used for each method.

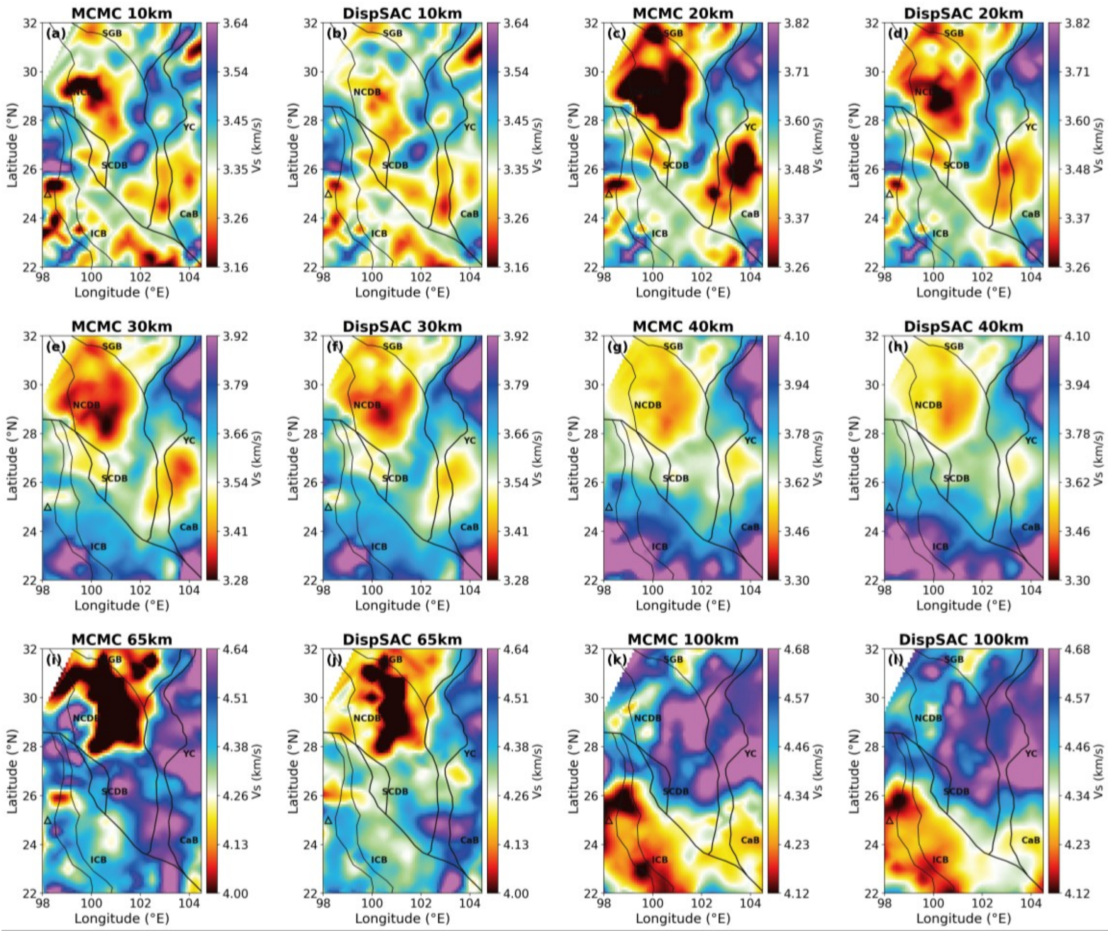

Figure 8 Comparison between MCMC inferred v_s model and DispSAC inferred v_s model across all

YunNan 393 stations in 10km, 20km, 30km, 40km, 65km, 100km.

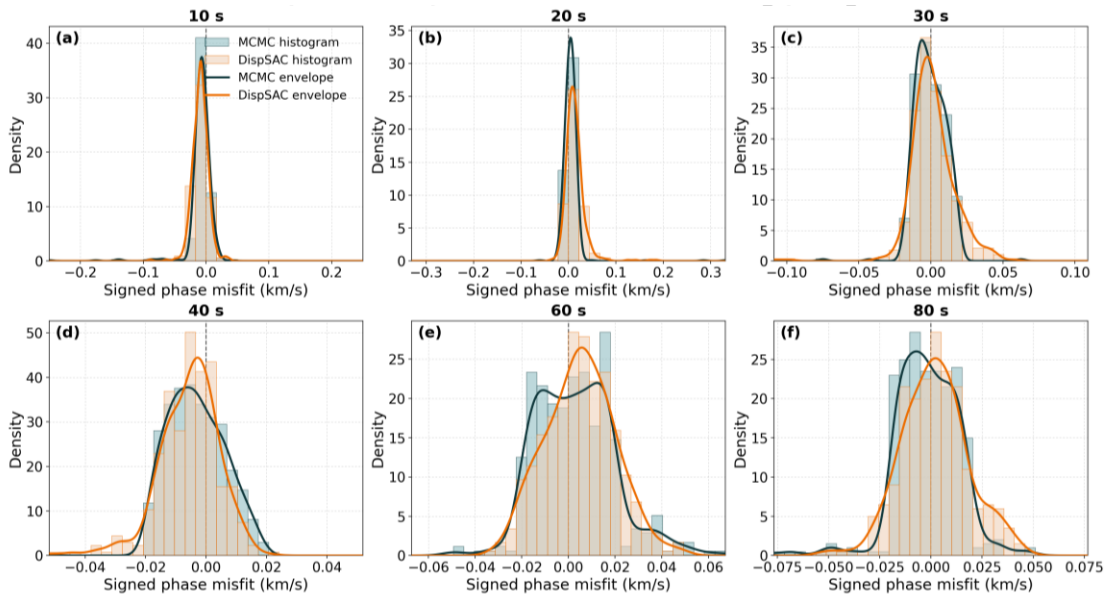

Figure 9 Histogram of MCMC phase misfits and DispSAC phase misfits in 10s, 20s, 40s, 60s, and 80s.

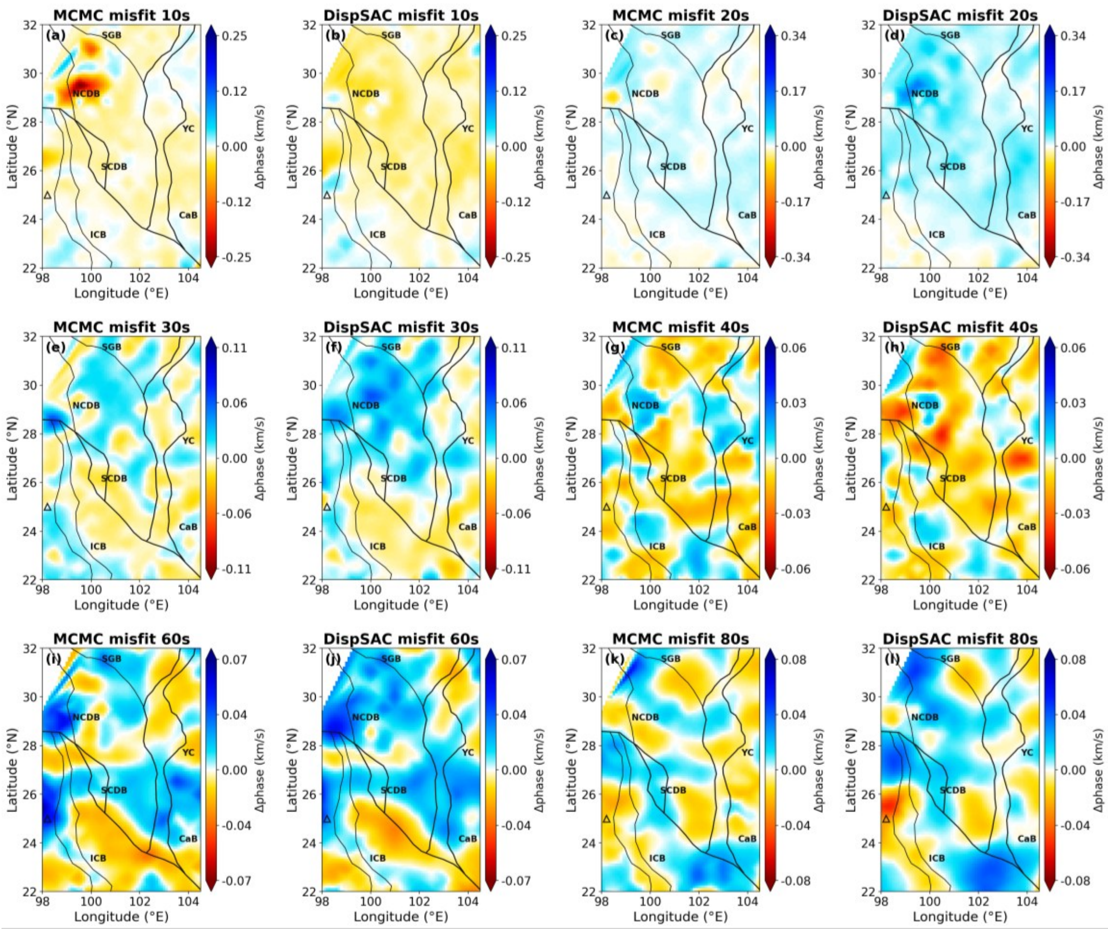

Figure 10 Comparison between MCMC phase misfit and DispSAC phase misfit across all YunNan 393 stations in 10s, 20s, 40s, 60s, and 80s. (a), (c), (e), (g), (i) and (k) means MCMC phase misfit; (b), (d),

(f), (h), (j) and (l) means DispSAC phase misfit.

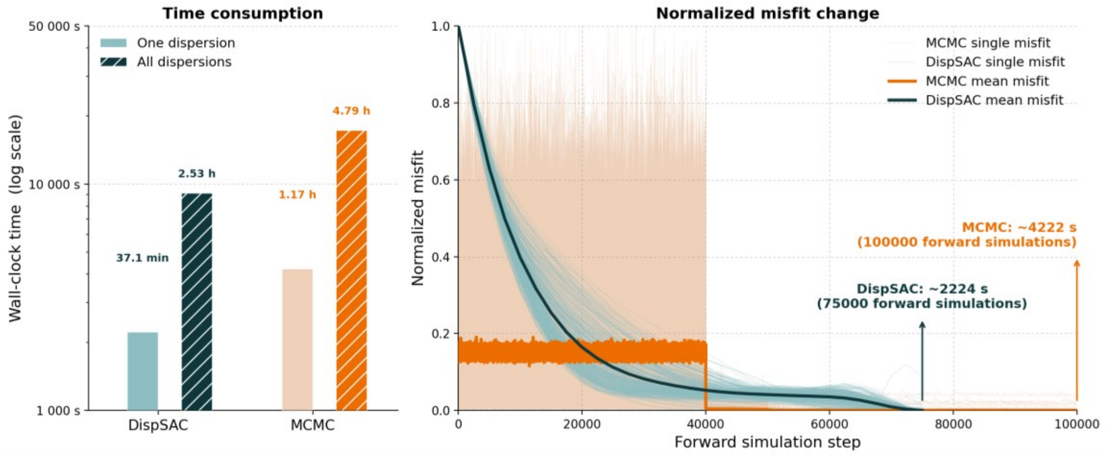

Figure 11 Efficency comparison between MCMC and DispSAC by inferring all YunNan dispersions.

Discussion

1. Comparison with MCMC

We also invert the western United States synthetic dispersion curves using MCMC to compare the two methods quantitatively. Because the velocity model used to generate these curves is known, model-recovery errors can be evaluated directly. We compare both the differences from the reference velocity model and the residuals between predicted and target dispersion.

The MCMC and DispSAC comparisons use the same B-spline coefficient bounds and summarize the inversions using 100 recovered models per target curve. Figure 12 compares the reference velocity field with the two sets of inferred velocity maps of different depths. Figure 13 compares the distributions of all velocity-model errors and phase-velocity residuals. DispSAC produces narrower distributions for the aggregate statistics. At individual depths, the relative performance of the methods varies, as illustrated by the distributions in Figure 13.

The runtime comparison in Figure 14 indicates shorter elapsed inference times for DispSAC in the displayed western United States experiment. A comparison of computational efficiency requires consistent definitions of the evaluation budget, stopping criterion, and retained output for both methods. The reported timings should therefore be interpreted for the specific benchmark configuration, with failure rates and the quality of the retained models assessed alongside elapsed time.

Figure 14 also shows the progression of dispersion misfit during inference. For DispSAC, 100 simultaneous inversion trajectories with 20 steps each correspond to 2,000 individual forward evaluations. Thus, a single trajectory step corresponds to 100 evaluations when results are combined across initializations. The normalized curves describe the relative evolution of each history. If each history is normalized separately, the curves do not provide a direct comparison of absolute final misfit between methods.

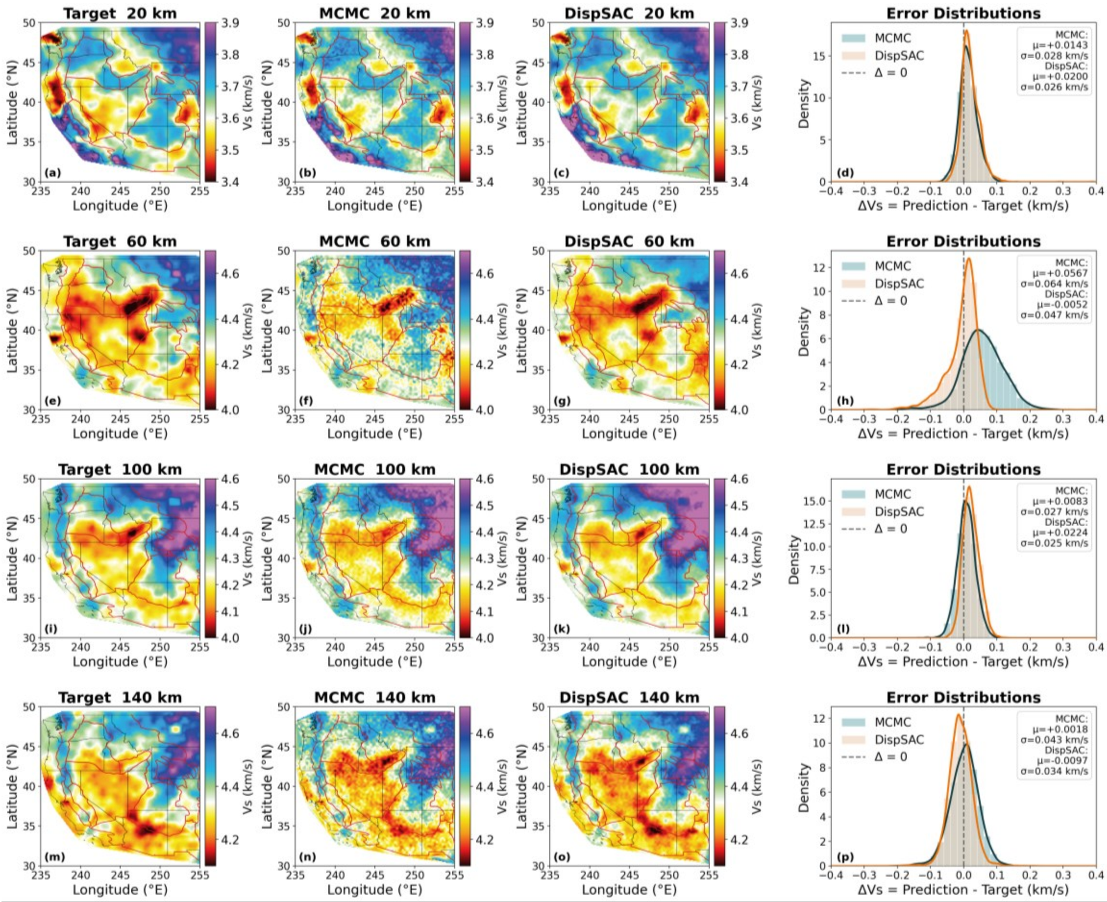

Figure 12 Comparison between target Western US v_s model and the MCMC inferred v_s model in 20km, 60km, 100km and 140km. First column: (a), (e), (i) and (m) means the Target Western US v_s model; Second column: (b), (f) , (j) and (n) means MCMC predictions; Third column: (c), (g), (k) and (o) mean DispSAC predictions. Fourth column: (d), (h), (l) and (p) is the difference distribution between target and prediction both for DispSAC and MCMC.

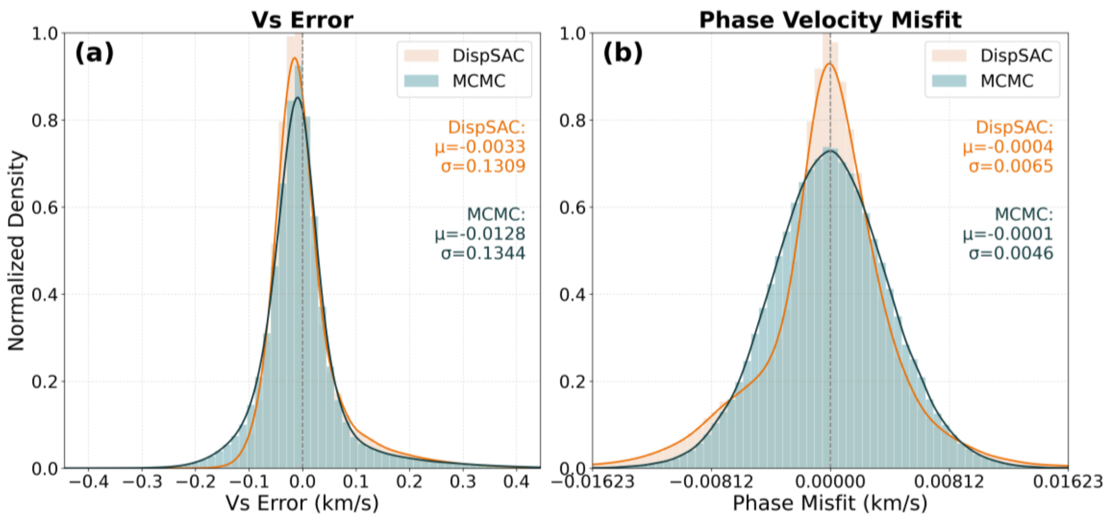

Figure 13 Comparing v_s error distribution and dispersion misfit distribution of DispSAC and MCMC.

(a) Distribution of the difference between target v_s and averaged predicted v_s; (b) Distribution of the difference between target Rayleigh phase velocity and averaged predicted Rayleigh phase velocity;

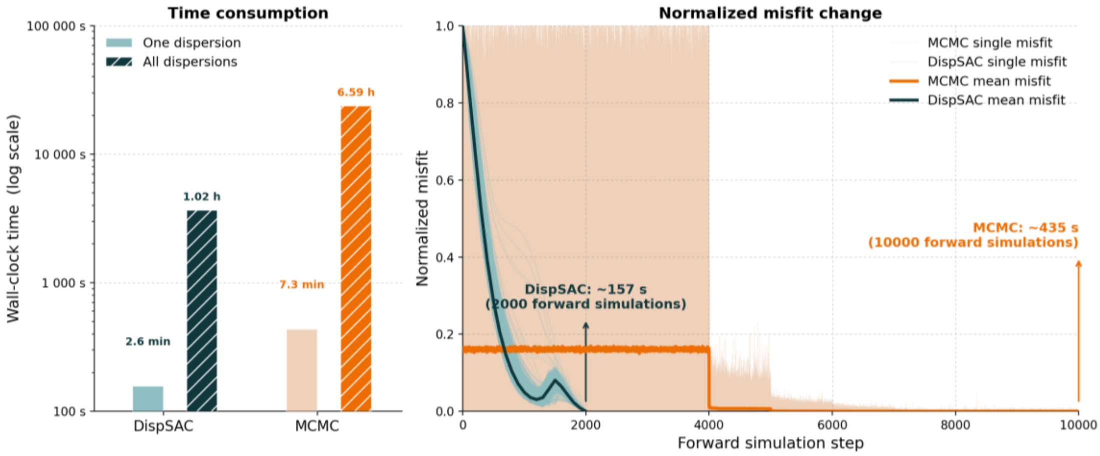

Figure 14 Comparing efficiency between MCMC and DispSAC when inferring synthetic Western US synthetic datasets. (a) Comparing time taken by DispSAC and MCMC. Slight colored histogram represents the time taken by one dispersion inference. The histogram with heavy color and slash lines represents the time taken by all dispersions' inferences; (b) DispSAC and MCMC evolution history. Slight line represents min-max normalized misfit change across iterations. One slight iteration curve means one dispersion inference. Thick line represents averaged min-max normalized misfit changes with iterations.

2. Mechanism Comparison between MCMC and DispSAC

Both DispSAC and MCMC generate sequences of model updates during inference, but their update mechanisms and objectives differ. Our MCMC implementation uses a single chain to sample the posterior distribution. Successive samples may be autocorrelated, potentially requiring a long run to obtain an adequate effective sample size. Its misfit can fluctuate because posterior sampling does not require a monotonic reduction in misfit. DispSAC instead performs multiple, relatively short inversion trajectories from different initial models, using a trained policy to guide each update toward improved data fit. Multiple initializations explore different starting regions, while the learned policy can reduce the number of updates needed to reach well-fitting models. Averaging across trajectories may also produce a smoother mean misfit history. These features offer potential computational advantages, although neither ensemble size nor smooth convergence alone establishes adequate coverage of the model space.

We simplify the mechanism of MCMC and DispSAC in the Figure 12. Parameter space is 10 dimensional space in this study but we simplify it into 2D circle plane, in which MCMC and DispSAC shows different mechanism in terms of searching strategy, posterior sampling, and computing efficiency.

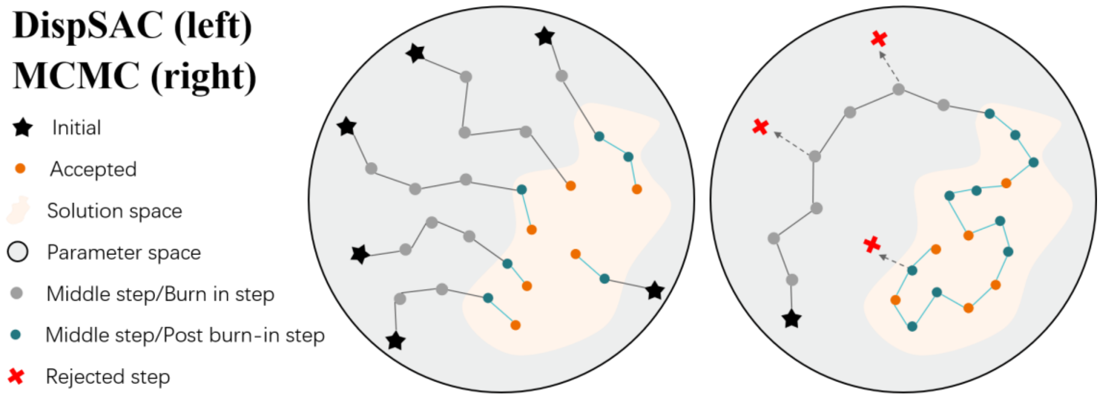

Figure 12 DispSAC and MCMC mechanism. DispSAC can be considered as a data assimilation process that can output totally independent accepted parameter vectors in ensemble. MCMC outputted accepted results are correlated because they are from the same chain.

3. Limitations and future work

Several limitations remain. Training performance can be sensitive to hyperparameter choices [36], and the appropriate rollout length may vary across target curves because the misfit does not necessarily decrease at every step. The B-spline parameterization and training distribution also restrict the structures that the agent can explore. Although the forward solver enforces the relationship between a candidate model and its dispersion, additional geological constraints or regularization may help control poorly resolved features. Finally, the spread of models recovered from multiple initializations requires further validation before it can be interpreted as calibrated uncertainty. Future work should examine stopping criteria, sensitivity to the training distribution, and the incorporation of complementary observations.

Conclusion

We present DispSAC, a method for estimating isotropic shear-wave velocity profiles from Rayleigh-wave dispersion using soft actor-critic reinforcement learning. The trained policy guides iterative updates of a B-spline model while a physical forward solver evaluates the fit to the target dispersion. Tests on synthetic and observed datasets demonstrate that the policy can be reused across locations and applied from multiple initial models. Comparisons with the implemented MCMC baseline indicate potential benefits in inference efficiency under the tested conditions, while also highlighting the need for consistent computational benchmarks. The recovered ensembles describe variability among the obtained solutions, but their interpretation as uncertainty requires further calibration. Future extensions could incorporate complementary geophysical data or connect dispersion extraction and usable-period selection with the inversion process.

Acknowledgement

We thank Xiaozhou Yang of China University of Geosciences, Wuhan, for providing the Yunnan dispersion data. We are grateful to Weiqiang Zhu and Erdinc Saygin for helpful discussions and suggestions, including those shared during the PIM2026 summer school.

Reference

[1] Yang, Shaobo, Haijiang Zhang, Zixin Chen, and Ying Liu. "Physics-informed neural networks for multi-period surface wave tomography." *Science China Earth Sciences* 68, no. 11 (2025): 3617-3629.

[2] Liu, Feng, Junlun Li, Lei Fu, and Laiyu Lu. "Multimodal surface wave inversion with automatic differentiation." *Geophysical Journal International* 238, no. 1 (2024): 290-312.

[3] Durand, S., E. Debayle, and Y. Ricard. "The lithosphere-asthenosphere system seen by surface waves: New insights from radial anisotropy." *Earth and Planetary Science Letters* 673 (2026): 119720.

[4] Zhao, Bing-kai, Yan-li Ding, Jia-qiang Song, Pei-yan He, and Shao-yuan Bai. "Inversion of rayleigh surface wave dispersion curves based on deep learning." *Applied Geophysics* (2025): 1-13.

[5] Wang, Feiyi, Xiaodong Song, and Mengkui Li. "A deep-learning-based approach for seismic surface-wave dispersion inversion (SfNet) with application to the Chinese mainland." *Earthquake Science* 36, no. 2 (2023): 147-168.

[6] Liu, Feng, Bao Deng, Rui Su, Lei Bai, and Wanli Ouyang. "DispFormer: A pretrained transformer incorporating physical constraints for dispersion curve inversion." *Journal of Geophysical Research: Machine Learning and Computation* 2, no. 3 (2025): e2025JH000648.

[7] Luo, Yinhe, Yao Huang, Yingjie Yang, Kaifeng Zhao, Xiaozhou Yang, and Hongrui Xu. "Constructing shear velocity models from surface wave dispersion curves using deep learning." *Journal of Applied Geophysics* 196 (2022): 104524.

[8] Meier, Ueli, Andrew Curtis, and Jeannot Trampert. "Global crustal thickness from neural network inversion of surface wave data." *Geophysical Journal International* 169, no. 2 (2007): 706-722.

[9] Yang, Jianxun, Chen Xu, and Ye Zhang. "Reconstruction of the s-wave velocity via mixture density networks with a new rayleigh wave dispersion function." *IEEE Transactions on Geoscience and Remote Sensing* 60 (2022): 1-13.

[10] Gai, Zicheng, and Yanfei Wang. "sFWI: physics-informed score-based generative modeling for robust full waveform inversion." *Machine Learning: Science and Technology* 7, no. 2 (2026): 025044.

[11] Colombo, Daniele, Ersan Turkoglu, Ernesto Sandoval-Curiel, and Taqi Alyousuf. "Self-supervised, active learning seismic full-waveform inversion." *Geophysics* 89, no. 2 (2024): U31-U52.

[12] Shen, Weisen, and Michael H. Ritzwoller. "Crustal and uppermost mantle structure beneath the

United States." *Journal of Geophysical Research: Solid Earth* 121, no. 6 (2016): 4306-4342.

[13] Dell'Aversana, P. "Combining geophysical inversion with Reinforcement Learning." In 83rd EAGE Annual Conference & Exhibition, vol. 2022, no. 1, pp. 1-5. European Association of Geoscientists & Engineers, 2022.

[14] Wang, Han, Yunhe Liu, Changchun Yin, Jinfeng Li, Yang Su, and Bin Xiong. "Stochastic inversion of magnetotelluric data using deep reinforcement learning." *Geophysics* 87, no. 1 (2022): E49-E61.

[15] Chang, Sung-Joon, Ana MG Ferreira, Jeroen Ritsema, Hendrik J. van Heijst, and John H. Woodhouse. "Joint inversion for global isotropic and radially anisotropic mantle structure including crustal thickness perturbations." *Journal of Geophysical Research: Solid Earth* 120, no. 6 (2015): 4278-4300.

[16] Liu, Feng, Sijie Zhao, Xinyu Gu, Fenghua Ling, Peiqin Zhuang, Yaxing Li, Rui Su et al. "OpenSWI: a massive-scale benchmark dataset for surface wave dispersion curve inversion." *Earth System Science Data* 18, no. 4 (2026): 2769-2798.

[17] Chang, Sung-Joon, Ana MG Ferreira, Jeroen Ritsema, Hendrik J. van Heijst, and John H. Woodhouse. "Global radially anisotropic mantle structure from multiple datasets: a review, current challenges, and outlook." *Tectonophysics* 617 (2014): 1-19.

[18] Becker, T. W. "Azimuthal seismic anisotropy constrains net rotation of the lithosphere." *Geophysical Research Letters* 35, no. 5 (2008).

[19] Cai, Ao, Hongrui Qiu, and Fenglin Niu. "Semi-supervised surface wave tomography with Wasserstein cycle-consistent GAN: Method and application to Southern California plate boundary region." *Journal of Geophysical Research: Solid Earth* 127, no. 3 (2022): e2021JB023598.

[20] Sutton, R. S., and A. G. Barto. 2018. Reinforcement Learning: An Introduction. 2nd ed. MIT Press.

[21] R. B. Herrmann, "Computer programs in seismology: An evolving tool for instruction and research," Seismological Research Letters, vol. 84, no. 6, pp. 1081–1088, 2013.

[22] Haarnoja, Tuomas, Aurick Zhou, Pieter Abbeel, and Sergey Levine. "Soft actor-critic: Off-policy maximum entropy deep reinforcement learning with a stochastic actor." In *International conference on machine learning*, pp. 1861-1870. Pmlr, 2018.

[23] Haarnoja, Tuomas, Aurick Zhou, Kristian Hartikainen, George Tucker, Sehoon Ha, Jie Tan, Vikash Kumar et al. "Soft actor-critic algorithms and applications." *arXiv preprint arXiv:1812.05905* (2018).

[24] D'Oro, Pierluca, Max Schwarzer, Evgenii Nikishin, Pierre-Luc Bacon, Marc G. Bellemare, and Aaron Courville. "Sample-efficient reinforcement learning by breaking the replay ratio barrier." In *Deep*

reinforcement learning workshop neurIPS 2022. 2022.

[25] Lillicrap, T. P., Hunt, J. J., Pritzel, A., Heess, N., Erez, T., Tassa, Y., Silver, D., and Wierstra, D. Continuous control with deep reinforcement learning. arXiv preprint arXiv:1509.02971, 2015.

[26] Schulman, J., Wolski, F., Dhariwal, P., Radford, A., and Klimov, O. Proximal policy optimization algorithms. arXiv preprint arXiv:1707.06347, 2017b.

[27] Bellman, Richard. "A Markovian decision process." *Journal of mathematics and mechanics* 6, no. 5 (1957): 679-684.

[28] Oh, Junhyuk, Yijie Guo, Satinder Singh, and Honglak Lee. "Self-imitation learning." In *International conference on machine learning*, pp. 3878-3887. PMLR, 2018.

[29] Schaul, Tom, John Quan, Ioannis Antonoglou, and David Silver. "Prioritized experience replay." *arXiv preprint arXiv:1511.05952* (2015).

[30] Dong, Qianyun, Hongrui Qiu, Jing Hu, Yong Zheng, Sanxi Ai, Siyuan He, and Lei Qin. "A Deep Learning-Based Forward Surrogate Model for Accelerating Surface-Wave Dispersion Inversion." *Seismological Research Letters* (2026).

[31] L. V. Socco and D. Boiero, “Improved monte carlo inversion of surface wave data,” Geophysical Prospecting, vol. 56, no. 3, pp. 357–371, 2008.

[32] M. Maraschini and S. Foti, “A monte carlo multimodal inversion of surface waves: Monte carlo multimodal surface wave inversion,” Geophysical Journal International, vol. 182, no. 3, pp. 1557–1566, 2010

[33] Hu, Jing, Hongrui Qiu, Haijiang Zhang, and Yehuda Ben-Zion. "Using deep learning to derive shear-wave velocity models from surface-wave dispersion data." *Seismological Research Letters* 91, no. 3 (2020): 1738-1751.

[34] X. Song, L. Tang, X. Lv, H. Fang, and H. Gu, “Application of particle swarm optimization to interpret rayleigh wave dispersion curves,” Journal of Applied Geophysics, vol. 84, pp. 1–13, 2012.

[35] M. Sambridge and K. Mosegaard, “Monte carlo methods in geophysical inverse problems,” Reviews of Geophysics, vol. 40, no. 3, 2002.

[36] Eimer, Theresa, Marius Lindauer, and Roberta Raileanu. "Hyperparameters in reinforcement learning and how to tune them." In *International conference on machine learning*, pp. 9104-9149. PMLR, 2023.

[37] N. M. Shapiro and M. H. Ritzwoller, “Monte-carlo inversion for a global shear-velocity model of

the crust and upper mantle," Geophysical Journal International, vol. 151, no. 1, pp. 88–105, 2002.

[38] Dell'Aversana, P. "Inversion of geophysical data supported by reinforcement learning." *Bulletin of Geophysics and Oceanography* 64, no. 1 (2023): 45-60.

[39] Sutton, Richard S., and Andrew G. Barto. *Reinforcement learning: An introduction*. Vol. 1, no. 1. Cambridge: MIT press, 1998.

[40] Brocher, T., 2005, Empirical relations between elastic wavespeeds and density in the Earth's crust: Bulletin of the Seismological Society of America, v. 95, no. 6, p. 2081-2092, https://doi.org/10.1785/0120050077.

[41] Bellman, Richard. "The theory of dynamic programming." *Bulletin of the American Mathematical Society* 60, no. 6 (1954): 503-515.